Supplementary Information for Ultrafast nano-imaging of electronic coherence of monolayer WSe_2

Wenjin Luo,[†,‡] Benjamin G. Whetten,[‡] Vasily Kravtsov,[¶] Ashutosh Singh,[§] Yibo Yang,[‖] Di Huang,[†] Xinbin Cheng,[†] Tao Jiang,[*,†] Alexey Belyanin,[*,§] and Markus B. Raschke[*,‡]

†*MOE Key Laboratory of Advanced Micro-Structured Materials, Shanghai Frontiers Science Center of Digital Optics, Institute of Precision Optical Engineering, and School of Physics Science and Engineering, Tongji University, Shanghai 200092, China*

‡*Department of Physics and JILA, University of Colorado, Boulder, CO, 80309, USA*

¶*ITMO University, Saint Petersburg, 197101, Russia*

§*Department of Physics and Astronomy, Texas A&M University, College Station 77843, Texas, United States*

‖*Department of Computer Science, University of Colorado, Boulder, CO, 80309, USA*

E-mail: tjiang@tongji.edu.cn; belyanin@physics.tamu.edu; markus.raschke@colorado.edu

February 19, 2023

Contents

Note 1: Micro-Raman and micro-PL spectroscopy

We perform micro-Raman and -PL spectroscopy to characterize and verify the monolayer and high quality nature of the WSe_2 sample used for the ultrafast nano-imaging experiments. Experiments are performed on a home-built micro-Raman/PL setup consisting of an upright microscope with an objective (Olympus, WD = 10.6 mm, 50×, NA = 0.5), and the signal is detected using a spectrometer (f = 500 mm, SpectraPro 500i, Princeton Instruments) with a thermoelectrically cooled charge-coupled device (ProEM+: 1600 eXcelon3, Princeton Instruments).

For WSe_2 and similar TMD structures, there are generally four Raman-active modes, namely the A_{1g}, E_{1g}, E^1_{2g} and E^2_{2g} modes.[1] Due to their forbidden selection rule in the far-field back-scattering geometry and the limited rejection against Rayleigh scattering, E_{1g} and E^2_{2g} are not observed in our measurements. The in-plane vibrational E^1_{2g} mode and out-of-plane vibrational A_{1g} mode are shown in Fig. S1a. We observed the E^1_{2g} mode at $\sim$250 cm^{-1} and the A_{1g} mode at $\sim$260 cm^{-1}. To distinguish the two modes, Voigt peaks (green solid line) were fitted to the measured spectrum (black solid line) to separate the E^1_{2g} mode (red dash line) and A_{1g} mode (blue dash line). To confirm the monolayer nature of the WSe_2 sample, the ratio of two peaks' intensities was extracted and determined to be 0.24, a value characteristic for monolayer WSe_2.[1]

Further, the photoluminescence (PL) spectrum (Fig. S1b) measured from a uniform area shows a single peak with emission centered at 750 nm, also characteristic for monolayer WSe_2.[2] The corresponding PL image (Fig. S1c) shows that the sample consists of a clean large monolayer region free of major micrometer scale heterogeneities.

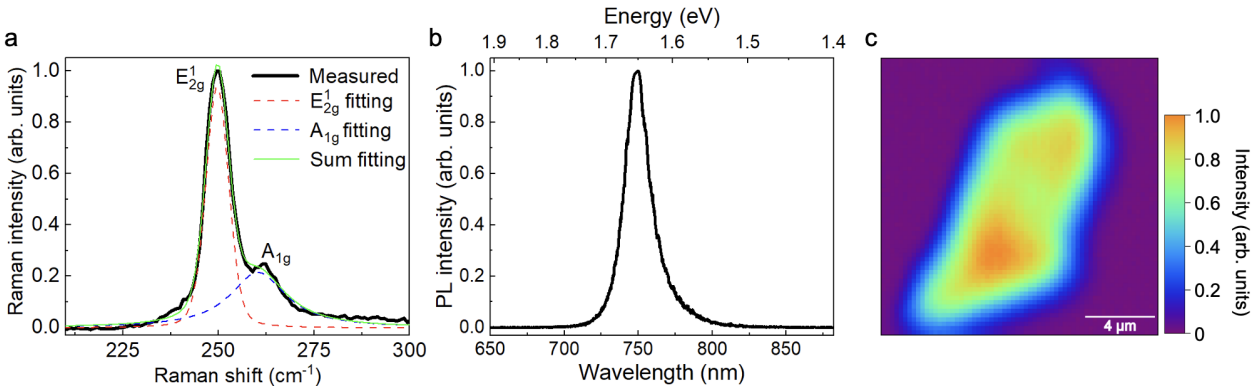

Fig. S1: (a) Micro-Raman spectrum of monolayer WSe_2 with E^1_{2g} and A_{1g} phonon modes, with Voigt fits, and 0.24 intensity ratio as characteristic for monolayer WSe_2 . (b) Corresponding micro-PL, centered at 750 nm for the direct bandgap monolayer emission of WSe_2 . (c) Micro-PL image of WSe_2 monolayer.

Note 2: AFM imaging

The corresponding tapping mode AFM image (Multimode 8, Bruker) of the WSe_2 sample used in the experiments is shown in Fig. S2a. The topography image shows a well defined flake with sharp edges, with several defects, folds, and contaminations resulting from the fabrication process. The red dashed rectangle shows the area selected for near-field imaging, as a nominally clean and smooth area avoiding folds, wrinkles, bubbles, and other features that can already be identified by AFM. The topographic line profile along the black line in the AFM image shows a ∼1.2 nm thickness for the WSe_2 monolayer.

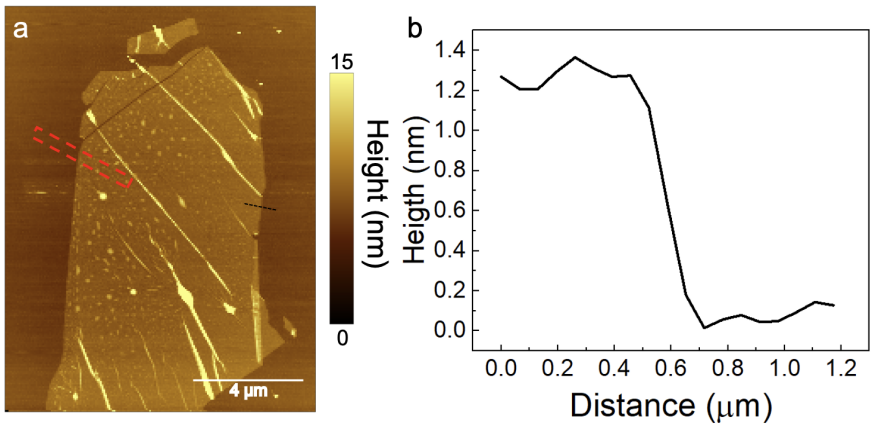

Fig. S2: (a) AFM topography of WSe_2 monolayer flake used in our work. (b) Line profile across the edge of the WSe_2 flake showing a ∼1.2 nm height.

Note 3: Line profiles of nano-SHG/2PPL/FWM images

To characterize the nano-scale, sub-wavelength, and sub-diffraction localization of the different nonlinear near-field signals, we show line profiles for the data from Fig. 2 from the main text. Figure S3a-c show the nonlinear optical (SHG, 2PPL, and FWM) nano-images (same as Fig. 2d-f in main text) and corresponding lines profiles along the black lines (Fig. S3d-f). The data indicate a spatial resolution of at least ∼60 nm, ∼90 nm and ∼90 nm, respectively, assuming the underlying features to be sharp, and as defined by the 10-90 % min-max standard established in the literature.[3] As discussed in the main text, a consistently higher near-field localization is observed for SHG compared to 2PPL and FWM. We attribute this to the high sensitivity of SHG to local inversion symmetry breaking compared to 2PPL and FWM. Figure S3g-i show the correlation analysis of near-field image signals (from Fig. 2d-f in the main text). As shown in Fig. S3g, the 2PPL and FWM signals present a vague positive correlation, possibly due to their common dependence on $\chi^{(3)}$. However, we do not identify a clear correlation either between 2PPL and SHG in Fig. S3h or between SHG and FWM in Fig. S3i, owing to the distinctive physical mechanisms involved in SHG, 2PPL, and FWM signals.

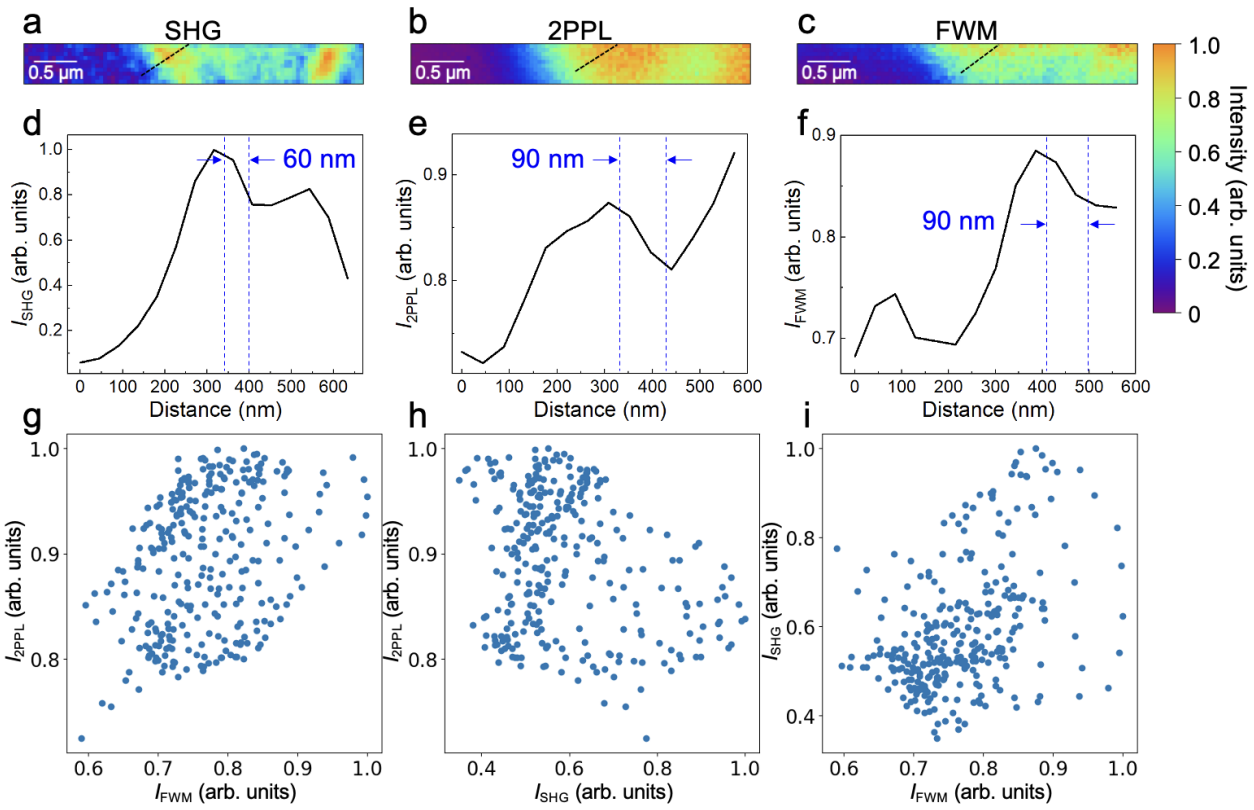

Fig. S3: (a-c) Nano-images of SHG, 2PPL, and FWM, with line profiles (black lines) indicating near-field localization to ∼60 nm for SHG (d), ∼90 nm for 2PPL (e) and ∼90 nm for FWM (f), respectively. (g-i) Correlation analysis between 2PPL and FWM(g), between 2PPL and SHG(h), and between SHG and FWM(i).

Note 4: FWM nano-imaging of decoherence

In addition to the exemplary data set in the main text, here we provide results from another measurement on a different sample equally pre-characterized as above, to demonstrate consistency of the results, most notably the anti-correlation of T_2 with FWM intensity.

To minimize the impact of sample drift, we merely performed subsequent line scans to investigate the temporal evolution of the near-field FWM two-pulse correlation measurements. Fig. S4a shows the FWM line profile across a heterogeneous sample region with corresponding spatial variations in FWM intensity. Similarly to the data in the main text, the signal decays on a 10's of fs timescale. Results from two representative sample locations are shown

in Fig. S4b.

In Fig. S4b the oscillations are the autocorrelation curves calculated from the two-pulse correlation model (see Note 6 below). We arbitrarily select the first (0 fs), third peaks (5.6 fs), and subsequent peaks (11.1, 13.8, 16.7 fs) as a compromise between the expected decoherence time and measurement time, including the time required to change the pulse delay and repeat the measurement of the FWM.

Here, spot A with high FWM intensity shows a decoherence time below the resolution limit of $\lesssim 5$ fs, while spot B with low FWM intensity shows $\sim$60 fs, i.e., again consistent with the trend discussed in the main text of higher initial FWM intensity at zero time delay associated with faster decoherence.

We further extract FWM intensity (from $\sim$0.6 to 1 arb. units) and the corresponding dephasing time (from $\lesssim$ 5 to 45 fs) from each pixel in the whole WSe_2 sample (301 data points in total), where 50 data points show weak FWM (from $\sim$0.6 to 0.7 arb. units) with long dephasing times (from $\sim$28 to 45 fs). On the other hand, among the whole data set, 73 data points show a dephasing time $\lesssim 5$ fs and a corresponding strong FWM intensity. If we average these 73 data points, we find that the dephasing time is $\sim$2 fs and the FWM intensity is 0.85 arb. units, showing a stronger FWM intensity relative to the rest of the data set.

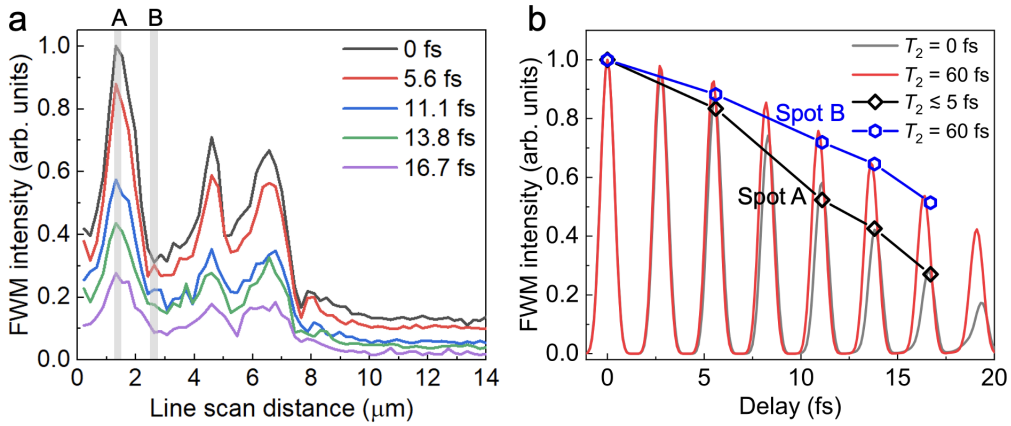

Fig. S4: (a) Line profile of temporal evolution of FWM intensity across structural features in monolayer WSe_2. (b) Analysis of representative sample locations exhibiting short decoherence times for high initial FWM intensity and vice versa. The black ($T_2 = 60$ fs) and red ($T_2 = 0$ fs) solid lines represent the calculated autocorrelation curves, while the black line with diamond symbol (Spot A, $T_2 \lesssim 5$ fs) and blue line with circle symbol (Spot B, $T_2 = 60$ fs) represent the autocorrelation data extracted from experiments.

Note 5: Dynamics of 2PPL signal

Similar to FWM, we perform a two-pulse correlation analysis of the 2PPL signal. In contrast to FWM, the 2PPL signal involves electronic dephasing process at the conduction band and population relaxation process from the conduction band to the excitonic state. As expected, Fig. S5 shows a distinct decay rate of 2PPL compared to that of FWM in WSe_2.

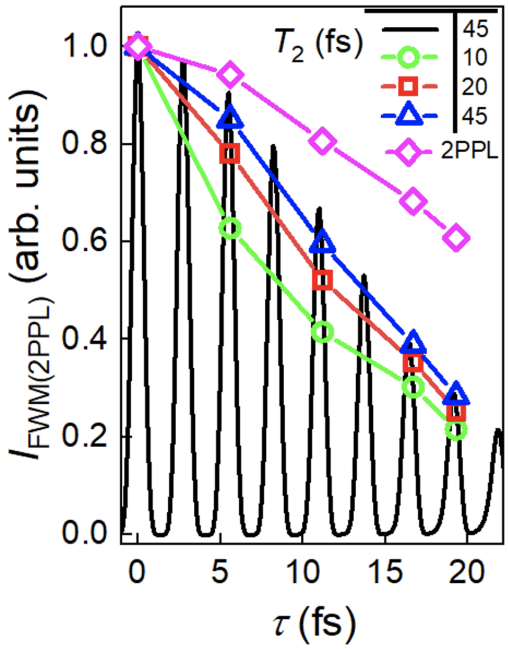

Fig. S5: 2PPL and FWM decay as a function of delay time. The 2PPL (pink curve) shows a much longer decay time than the FWM for dephasing times of 10 fs (green), 20 fs (red), and 45 fs (blue).

Note 6: Two-pulse correlation model

This section describes the calculation of the two-pulse correlation trace as a function of the delay between two pulses. With time delay τ and fundamental excited electric field $\tilde{E}(\omega)$, the two-pulse interferometric electric field can be expressed as:

$$\tilde{E}_{2-\text{pulse}}(\omega,\tau) = \int_{-\infty}^{\infty} [\tilde{E}(t) + \tilde{E}(t-\tau)] \exp(-i\omega t)\mathrm{d}t = 2\tilde{E}(\omega) cos(\omega\tau/2) e^{-i\omega\tau/2} \qquad (1)$$

In the experiment, we optimize the phase of the field spectrum to 0, so that $\tilde{E}(\omega) = \sqrt{I(\omega)}$, where $I(\omega)$ is the laser spectrum as measured with the spectrometer.

The third-order susceptibility is given by

$$\chi^{(3)}(-\omega;\omega_1,-\omega_2,\omega_3) \propto [D(\omega)D(\omega_1)D(-\omega_2)D(\omega_3)]^{-1} \qquad (2)$$

with the $D(\omega_j) = \omega_0^2 - \omega_j^2 - 2i\omega_j/T_2$, where $\omega_0 = 1.57\,\mathrm{eV}$ is the resonance energy of FWM in our case.

From the expression for third-order susceptibility $\chi^{(3)}$ (see, e.g. 3.7.10 from Boyd, Nonlinear Optic, third edition), its magnitude is determined by the optical dipole moments, detunings, and dephasing times of the optical transitions closest to the excitation spectrum. As discussed below (Note 7 FWM pathways) from comparison with MoS_2 , our FWM response in WSe_2 is resonantly enhanced by the A-exciton thus reflecting its coherence time.

The spectral intensity I_{FWM} of the generated FWM signal is calculated from the 2-pulse interferometric response electric field $E_{\text{2-pulse}}(\omega, \tau)$, with all possible frequencies ω_1, ω_2, and ω_3 within its bandwidth:

$$I_{\mathrm{FWM}}(\omega,\tau) \propto \left| \iiint_{-\infty}^{\infty} d\omega_{i=1,2,3} \chi^{(3)}(\omega;\omega_1,\omega_2,\omega_3) \right. \\ \left. \tilde{E}_{\text{2-pulse}}(\omega_1,\tau)\tilde{E}^{\star}_{\text{2-pulse}}(\omega_2,\tau)\tilde{E}_{\text{2-pulse}}(\omega_3,\tau)\delta(\omega-\omega_1+\omega_2-\omega_3) \right|^2 \tag{3}$$

We determine the total FWM intensity as a function of delay time τ by integrating over ω:

$$I_{\mathrm{FWM}}(\tau) \propto \int I_{\mathrm{FWM}}(\omega,\tau) d\omega \tag{4}$$

By varying τ, we obtain the FWM intensity traces as shown in the main text (Fig. 3b, gray line). Finally, we compare the experimentally measured FWM intensities $I_i(\tau)$, with calculated FWM intensities $I_{\mathrm{FWM}}(\tau)$, for assorted T_2 values and minimize the residual $r = \sum_i |I_{\mathrm{FWM}} - I_i|$ to determine T_2 for the experimental data.

Note 7: FWM identification and pathways

FWM identification:

We assign the spectral peak from 750 to 770 nm in Fig. 1b to FWM for several reasons.

Importantly, the signal exhibits a third-order power dependence as shown in Fig. 1d in the main text.

Additionally, the observed FWM spectrum can be fully derived from the shape of the pump spectrum using Eq. 3 in Note 6 (also see Ref. [4]). We compare this calculated spectrum with the measured WSe_2 spectrum by isolating the FWM peak from the 2PPL signal (distinctly identified by its second order power dependence) through fitting the complete spectrum with a double Voigt function. The calculated spectrum (blue dashed line) is in excellent agreement with the experimental FWM spectrum Voigt peak (red dashed line), as shown in Fig. S6.

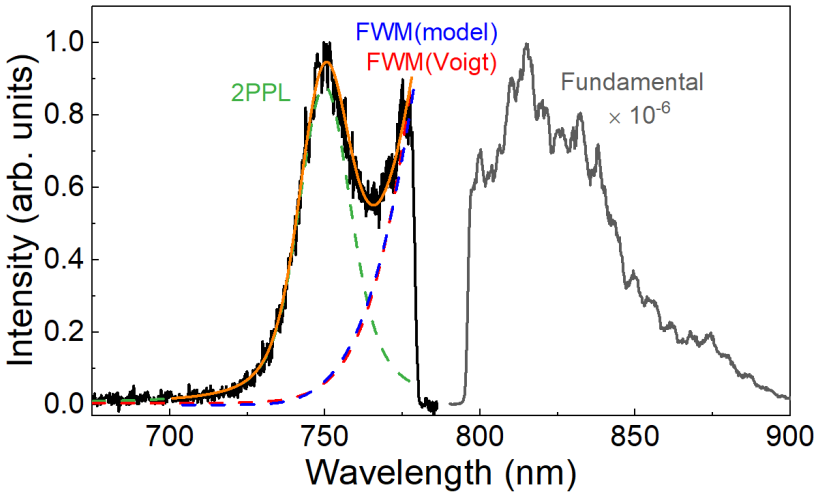

Fig. S6: FWM(Voigt) based on Voigt fitting *vs* FWM(model) based on Eq. 3 in Note 6 (also Eq. 1 in Ref. [4]). The calculated FWM spectrum (blue dashed) based on Eq. 3 is in excellent agreement with the data and again verifies the correct signal identification as FWM.

The spectral FWM characteristics are also in full agreement with previous work by us[4–6] and others.[7–10]

FWM pathways:

To confirm that the strong FWM signal of our WSe_2 sample is due to enhancement via the A-exciton through the triply degenerate pathway (Fig. 1c, left pathway), we compare

the FWM intensity of monolayer MoS_2 with WSe_2 under the same experimental conditions using far-field excitation (Fig. S7). WSe_2 (red) shows both strong A-exciton derived 2PPL and FWM. In contrast, MoS_2 only shows a weak FWM response (black) and no 2PPL due to its larger bandgap and exciton resonance at 1.85 eV (670 nm).[11,12] If the right pathway in Fig. 1c dominated the FWM response, then the intensity and spectral characteristics of the signal from MoS_2 and WSe_2 would be similar. However, WSe_2 clearly shows increased FWM response over MoS_2 and therefore the strong FWM in our WSe_2 is due to the triply degenerate single-photon resonant transition with the A-exciton (Fig. S7a, blue box).

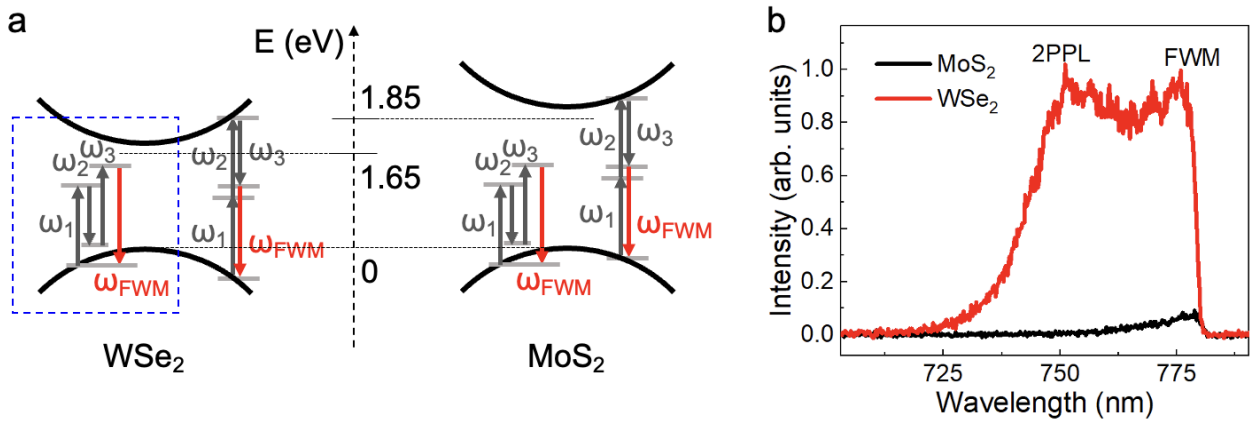

Fig. S7: (a) The band structures of WSe_2 and MoS_2 with their A-exciton positions indicated. (b) The FWM spectrum from monolayer WSe_2 and monolayer MoS_2 under the same excitation far-field conditions.

The enhancement of the FWM in WSe_2 is due to the A-exciton peak being detuned by from the FWM by only 1.9 FWHW (83.7 meV/44 meV). Because of its large oscillitor strength and the lack of other transitions near the FWM the A-exciton dominates over any other pathway. Because the A-exciton is the main contributor to the FWM polarization, the dephasing rate of the FWM polarization is dependent on the dephasing rate of the A-exciton.

References

(1) Zeng, H.; Liu, G.-B.; Dai, J.; Yan, Y.; Zhu, B.; He, R.; Xie, L.; Xu, S.; Chen, X.; Yao, W., et al. Optical signature of symmetry variations and spin-valley coupling in atomically thin tungsten dichalcogenides. *Sci. Rep.* **2013**, *3*, 1608.

(2) Seyler, K. L.; Schaibley, J. R.; Gong, P.; Rivera, P.; Jones, A. M.; Wu, S.; Yan, J.; Mandrus, D. G.; Yao, W.; Xu, X. Electrical control of second-harmonic generation in a WSe2 monolayer transistor. *Nat. Nanotechnol.* **2015**, *10*, 407–411.

(3) Hunsche, S.; Koch, M.; Brener, I.; Nuss, M. THz near-field imaging. *Opt. Commun.* **1998**, *150*, 22–26.

(4) Kravtsov, V.; Ulbricht, R.; Atkin, J. M.; Raschke, M. B. Plasmonic nanofocused four-wave mixing for femtosecond near-field imaging. *Nat. Nanotechnol.* **2016**, *11*, 459–464.

(5) Jiang, T.; Kravtsov, V.; Tokman, M.; Belyanin, A.; Raschke, M. B. Ultrafast coherent nonlinear nanooptics and nanoimaging of graphene. *Nat. Nanotechnol.* **2019**, *14*, 838–843.

(6) Kravtsov, V.; AlMutairi, S.; Ulbricht, R.; Kutayiah, A. R.; Belyanin, A.; Raschke, M. B. Enhanced third-order optical nonlinearity driven by surface-plasmon field gradients. *Phys. Rev. Lett.* **2018**, *120*, 203903.

(7) Min, W.; Lu, S.; Rueckel, M.; Holtom, G. R.; Xie, X. S. Near-degenerate four-wave-mixing microscopy. *Nano Lett.* **2009**, *9*, 2423–2426.

(8) Selm, R.; Krauss, G.; Leitenstorfer, A.; Zumbusch, A. Simultaneous second-harmonic generation, third-harmonic generation, and four-wave mixing microscopy with single sub-8 fs laser pulses. *Appl. Phys. Lett.* **2011**, *99*, 181124.

(9) Pearson, B.; Weinacht, T. Three-in-one microscopy. *Nat. Photon.* **2012**, *6*, 78–80.

(10) Kumar, S.; Kamali, T.; Levitte, J. M.; Katz, O.; Hermann, B.; Werkmeister, R.; Považay, B.; Drexler, W.; Unterhuber, A.; Silberberg, Y. Single-pulse CARS based multimodal nonlinear optical microscope for bioimaging. *Opt. Express* **2015**, *23*, 13082–13098.

(11) Mak, K. F.; Lee, C.; Hone, J.; Shan, J.; Heinz, T. F. Atomically thin MoS_2: a new direct-gap semiconductor. *Phys. Rev. Lett.* **2010**, *105*, 136805.

(12) Splendiani, A.; Sun, L.; Zhang, Y.; Li, T.; Kim, J.; Chim, C.-Y.; Galli, G.; Wang, F. Emerging photoluminescence in monolayer MoS_2. *Nano Lett.* **2010**, *10*, 1271–1275.